Acta Pharmaceutica Sinica B 2025;15(8):4285−4299

Chinese Pharmaceutical Association
Institute of Materia Medica, Chinese Academy of Medical Sciences

Acta Pharmaceutica Sinica B

www.elsevier.com/locate/apsb
www.sciencedirect.com

ORIGINAL ARTICLE

Rapid discovery of drug-introduced multiple organ dysfunction *via* NIR-II fluorescent imaging

Pu Jiang[a,b,c], Ruihu Song[c], Yue Hu[a,c], Xin He[a,b,c], Zewei Zhang[a,c], Xuemei Wei[c], Zhiming Wang[c,*], De-an Guo[a,b,*], Hao Chen[a,c,*]

[a]*School of Pharmacy, Nanjing University of Chinese Medicine, Nanjing 210023, China*
[b]*Shanghai Research Center for Modernization of Traditional Chinese Medicine, National Engineering Research Center of TCM Standardization Technology, Shanghai Institute of Materia Medica, Chinese Academy of Sciences, Shanghai 201203, China*
[c]*State Key Laboratory of Chemical Biology, Molecular Imaging Center, Shanghai Institute of Materia Medica, Chinese Academy of Sciences, Shanghai 201203, China*

Received 15 December 2024; received in revised form 8 April 2025; accepted 10 May 2025

KEY WORDS

Drug side effect;
Multiplexed imaging;
Aristolochic acids;
NIR-II imaging;
Hemicyanine dyes;
Liver injuries;
Kidney injuries;
Gastric dysfunction

Abstract The precise and rapid monitoring of multiple organ dysfunction is crucial in drug discovery. Traditional methods, such as pathological analysis, are often time-consuming and inefficient. Here, we developed a multiplexed near-infrared window two (NIR-II) fluorescent bioimaging method that allows for real-time, rapid, and quantitative assessment of multiple organ dysfunctions. Given that existing probes did not fully meet requirements, we synthesized a range of NIR-II hemicyanine dyes (HDs) with varying absorption and emission wavelengths. By modifying these dyes, we achieved high spatial and temporal resolution imaging of the liver, kidneys, stomach, and intestines. This method was further applied to investigate disorders induced by cisplatin, a drug known to cause gastric emptying issues along with liver and kidney injuries. By monitoring the metabolic rate of the dyes in these organs, we accurately quantified multi-organ dysfunction, which was also confirmed by gold-standard pathological analysis. Additionally, we evaluated the effects of five aristolochic acids (AAs) on multiple organ dysfunction. For the first time, we identified that AA-I and AA-II could cause gastric emptying disorders, which was further validated through transcriptomics analysis. Our study introduces a novel approach for the simultaneous monitoring of multi-organ dysfunction, which may significantly enhance the evaluation of drug side effects.

*Corresponding authors.
E-mail addresses: zmw@simm.ac.cn (Zhiming Wang), daguo@simm.ac.cn (De-an Guo), haoC@simm.ac.cn (Hao Chen).

Peer review under the responsibility of Chinese Pharmaceutical Association and Institute of Materia Medica, Chinese Academy of Medical Sciences.

https://doi.org/10.1016/j.apsb.2025.06.023

1. Introduction

The side effects of drug-related incidents are vital contributors to the failure of drug development or the withdrawal of medications[1]. The liver, kidneys, and gastrointestinal system, being the primary metabolic organs in the human body, are critical areas where adverse reactions often occur[2-4], including the anticancer drug cisplatin and the pain reliever acetaminophen, have been associated with various side effects on these organs[5,6]. In addition, the treatment of complex diseases often involves multiple medications, which can further harm the liver, kidneys, and gastrointestinal system. Clinically, these side effects can lead to serious health complications and increased mortality risk[7]. Thus, early detection of toxicities is crucial for implementing timely protective measures to prevent more severe issues. Unfortunately, current diagnostic methods mainly rely on serological biomarkers (*e.g.*, kidney: serum creatinine (SCr), blood urea nitrogen (BUN); liver: aspartate aminotransferase (AST), alanine aminotransferase (ALT); stomach: gastrin 17, pepsinogen I/II), endoscopic, radiological tests (barium X-ray imaging), and histological examinations[8-10]. However, endoscopy is invasive and may deter patients from undergoing tests, while radiography poses risks of ionizing radiation exposure[11]. Moreover, serological biomarkers often lack specificity and accuracy, failing to provide real-time diagnostic and prognostic information. Therefore, there is an urgent need for the development of dynamic, noninvasive methods to detect potential multi-organ toxic side effects of drugs, which would help mitigate risks in drug development.

Optical molecular imaging is crucial for noninvasive and real-time observation of disease progression and treatment responses in living organisms[12-14]. Specifically, fluorescence imaging in the second near-infrared window (NIR-II, 1000−1700 nm) offers deeper tissue penetration, reduced absorption, and less photon scattering, resulting in improved image quality[15,16]. Recently, the advancements in optical molecular imaging technology have accelerated due to its high sensitivity, affordability, and facile operation. For example, surgical removal of primary and metastatic liver tumors has been successfully conducted using the dye indocyanine green[17], renal clearance kinetics have been directly monitored in live mice with glutathione-modified gold nanoparticles[18], and azole compounds have been utilized for *in vivo* gastrointestinal imaging, allowing for dynamic tracking of gastric emptying and serving as a reference for assessing anti-acid treatments[19]. Although promising results have been achieved, most optical probes are tailored to target specific organs, leading to information gaps and impacting the accuracy of drug toxicity assessments. Given the frequent adverse reactions in multiple organs associated with clinically used drugs, there is a need for the development of molecular probes and technologies capable of simultaneously monitoring two or more organs to gain a more comprehensive understanding of drug effects.

In vivo multiplexed fluorescence imaging in the NIR-II range is a high-throughput analysis method that significantly decreases both time and sample size, offering a promising method for the simultaneous observation of various organs, tissues, and biomarkers[20-22]. Typically, fluorescent probes used for multiplexed imaging need to have easily adjustable structures to create fluorophores with different absorption and emission spectra. They must have excellent fluorescence intensity to ensure imaging effectiveness and possess well-defined absorption/emission spectral peaks to minimize spectral crosstalk[20,23-25]. These stringent spectral requirements limit the fluorescent dyes available for NIR-II multicolor imaging. Currently, the most common tunable wavelength NIR-II dyes include cyanine, boron dipyrromethene (BODIPY), and donor−acceptor−donor (D-A-D) compounds[26-28]. However, D-A-D dyes usually have low quantum yields and broad absorption spectra, which are prone to spectral overlap[29-31]. BODIPY derivatives face the drawback of a small Stokes shift, which can result in self-quenching and measurement inaccuracies due to excitation and scattered light[32,33]. In contrast, cyanines typically have a higher molar extinction coefficient and better biocompatibility, making them ideal candidate probes. They consist of a long conjugated methine chain and two symmetric or asymmetrical heterocyclic terminal moieties[34]. So far, a variety of commercial cyanine dyes with symmetrical structures, including ICG, IRDye800CW, IR12N3, and IR-775/808/797, have been developed for imaging the liver, brain, kidney, and other tissues[35-37]. Compared with symmetrical cyanins, asymmetric hemicyanines characteristic of a donor−π−acceptor (D−π−A) motif possess higher quantum yields and better structural flexibility[38-42]. Unfortunately, most reported hemicyanine dyes (HDs) have limited spectral differentiation[39,43]. It is urgent to design a reasonable molecular modification strategy to meet the requirements of multicolor imaging.

In this study, we created a series of spectrally harmonizable HD libraries with emission wavelengths between 674 and 1145 nm by expanding the conjugated system, replacing heteroatoms, and modifying various substitution patterns. We also employed rational molecular engineering to merge the HD3 fluorophore fragment with a renal clearance-enhancing functional fragment (mono-(6-(1,6-hexamethylenediamine)-6-deoxy)-β-cyclodextrin) to create HD3-CD, which exhibits both hepatic and renal clearance properties. This allowed us to perform real-time, noninvasive NIR-II imaging to assess cisplatin-induced liver and kidney dysfunction (Fig. 1A). Additionally, we identified the acid-resistant HD6 and HD14 with an emission wavelength of over 1100 nm to evaluate the cisplatin-induced damage in the stomach and intestines (Fig. 1B). Based on this, we further established a multi-channel bio-imaging platform for monitoring the liver, kidneys, stomach, and intestines, leveraging the excellent spectral differentiation of HD6, HD3-CD, and HD14 under 660, 808, and 915 nm lasers (Fig. 1C). This multicolor imaging technique was employed for the first time to identify potential gastric emptying disorders caused by aristolochic acid I (AA-I) and aristolochic acid II (AA-II), which were further confirmed through transcriptomics analysis (Fig. 1D).

2. Materials and methods

2.1. Materials characterization

^{1}H and ^{13}C spectra were recorded on Bruker Avance Neo 500 (Karlsruhe, Germany). Matrix-assisted laser desorption

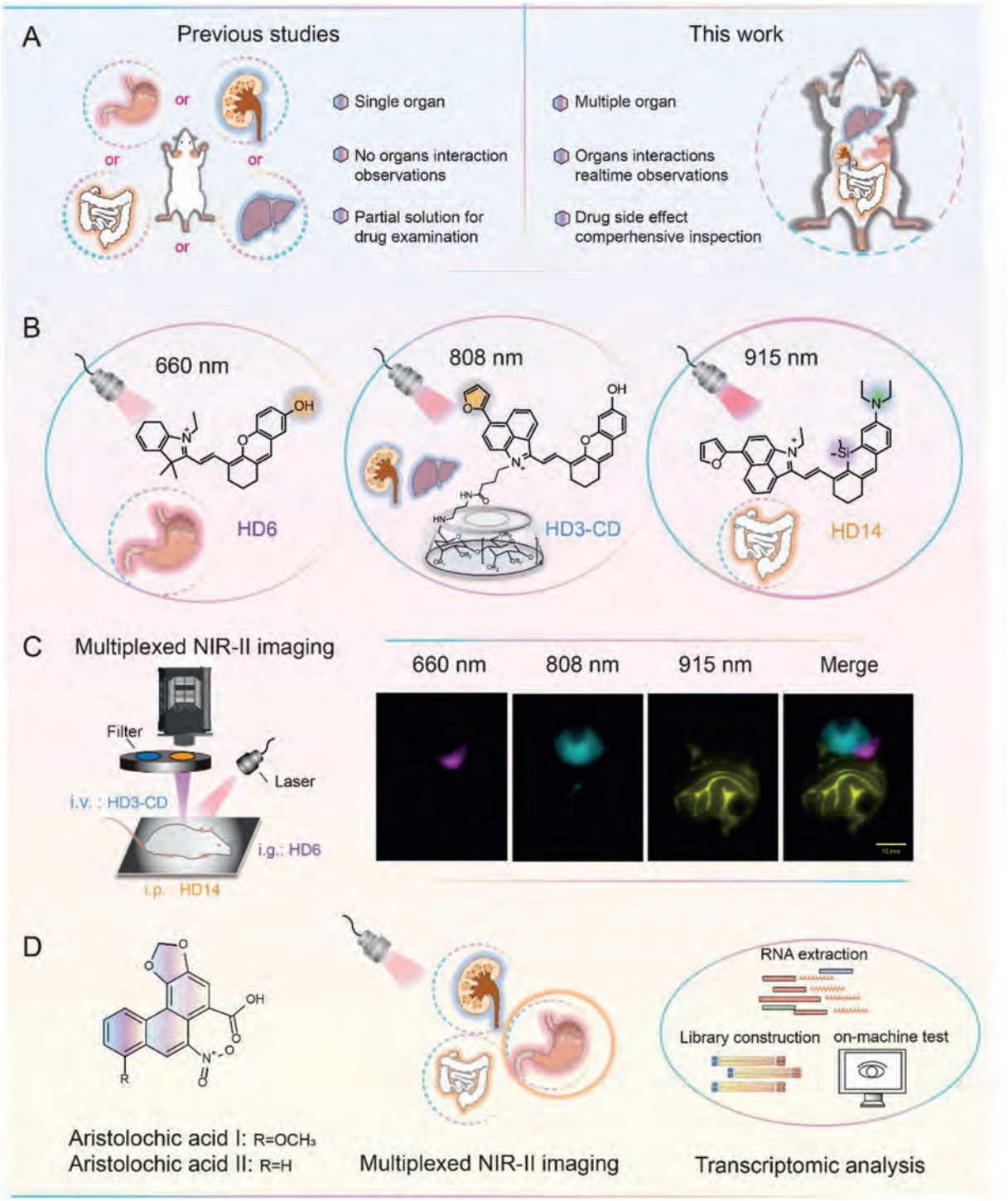

Figure 1 Design of multiplexed NIR-II imaging platform for monitoring drug-induced multiple organ dysfunction. (A) Comparison of multiplexed NIR-II imaging and traditional imaging. (B) NIR-II imaging of Cisplatin-induced liver, kidney, stomach, and intestinal disorders, respectively. (C) Establishment of a multiplexed NIR-II imaging platform. (D) Monitoring AAs toxicity with a multiplexed NIR-II imaging platform. i.v.: intravenous injection, i.p.: intraperitoneal injection, i.g.: intragastric gavage. Scale bar = 10 mm.

time-of-flight mass spectroscopy (MALDI-TOF-MS) was collected on Bruker AutoFlex Max (Karlsruhe, Germany). Electron spray ionization low resolution (ESI-LR) was performed on a Finnigan LTQ and Waters SQ Detector (Milford, MA, USA). High-resolution mass spectra (HRMS) were recorded using a Thermo Scientific Q Exactive Plus spectrometer (Waltham, MA, USA). Absorbance spectra were obtained by a Shimadzu Ultraviolet−Visible-2600 spectrometer (Tokyo, Japan). Emission spectra were obtained by Artemis Intelligent Imaging MARS-IRIS (Shanghai, China) and Techcomp Fluorescence Spectrometer FL960 (Beijing, China). The NIR-II fluorescence images were performed on Artemis Intelligent Imaging MARS (Shanghai,

China). The high-performance liquid chromatography (HPLC) data were acquired using a Thermo UltiMate 3000 HPLC system (Waltham, MA, USA).

2.2. Chemicals and biological reagents

All chemicals were purchased from Bide Pharmatec (Shanghai, China), Aladdin Bio-Chem Technology (Shanghai, China), and Macklin Biochemical (Shanghai, China) unless otherwise stated. Indocyanine green (CAS#: 3599-32-4) was purchased from Chem-Impex International Co., Ltd. (Shanghai, China). Cisplatin (CAS#: 15663-27-1) was obtained from Qilu Pharmaceutical Co., Ltd. (Jinan, China). Aristolochic acid I (CAS#:313-67-7), aristolochic acid II (CAS#:475-80-9), aristolochic acid IIIa (CAS#:4849-90-5), aristolochic acid IVa (CAS#: 17413-38-6), aristolochic lactam I (CAS#:13395-02-3) were purchased from Nature Standard Co., Ltd. (Shanghai, China). β-Actin (No. 20536-1-AP) and BAX (No. 50599-2-Ig) were purchased from Proteintech Co., Ltd. (Wuhan, China). TGF-β1 (No. HA721143) and SMAD3 (No. ET1607-41) were purchased from HUABIO Co., Ltd. (Hangzhou, China). NF-κB and NLRP3 were purchased from Cell Signaling Technology Co., Ltd. (Danvers, MA, USA). Non-fluorescent interference mouse feed was purchased from Synergy Medical Bioengineering Co., Ltd. (Nanjing, China).

2.3. Synthesis

For all synthesis details, please see the Supporting Information.

2.4. Quantum yield (Φ) calculations

The fluorescence quantum yields of HD1−13 in MeOH were determined from the relative fluorescence quantum yields by comparing with the IR140 (Φ = 16.7% in ethanol) as the reference; HD3-CD in H_2O, HD14 in MeOH were determined from the relative fluorescence quantum yields by comparing with the IR26 (Φ = 0.5% in 1,2-dichloroethane (DCE)). The quantum yields were calculated as shown in Eq. (1):

$$QY_{sample} = QY_0 \times \frac{Slope_{sample}}{Slope_0} \times \left(\frac{n_{sample}}{n_0}\right)^2 \quad (1)$$

where subscripts "sample" and "0" represent sample and reference, respectively. The slope is the slope of the integrated fluorescence intensity against the absorbance plot (linear fitting). "n" is the refractive index of the solvent. The maximal absorptions of all samples were carefully controlled to be lower than 0.1 for all measurements to eliminate self-quenching or re-absorption/re-emission issues. The sample and reference were excited by the same laser (HD1, HD6, 645 nm; HD2−5, HD7−13, 660 nm; HD3-CD, 808 nm; HD14, 980 nm).

2.5. Establishment of a mouse model

Female BALB/c mice (6 weeks old) were purchased from the Shanghai Experimental Animal Center (Shanghai, China). Mice were raised under pathogen-free conditions and allowed free access to food and water without fluorescent interference. All animal experiments were carried out in accordance with the National Institutes of Health guide for the care and use of Laboratory animals (NIH Publications No. 8023, revised 1978) and approved by the Institutional Animal Care and Use Committee (IACUC) of the Shanghai Institute of Materia Medica, Chinese Academy of Sciences. Drug-induced organ injury models were established by intraperitoneal injection with cisplatin (20 mg/kg body weight) or oral gavage with AAs (20 mg/kg body weight, once a day for 6 days). AAs were dissolved in 0.5% CMC-Na (Aladdin Bio-Chem Technology, Shanghai, China) solvent and stored at 4 °C before use.

2.6. pH stability test

HDs (5 μL, dissolved in MeOH) solvent was incubated with pretreated PBS (1 mL) of different pH values for 30 min and analyzed by ultraviolet−visible-2600 spectrometer (Shimadzu).

2.7. Determination of dye purity

Chromatographic separation was performed using an Agilent EclipseXDB C18 column (4.6 mm × 150 mm, 5 μm), with 0.1% methanol (solvent A) and water containing 0.1% (*v*/*v*) formic acid (solvent B) as the mobile phases. A gradient elution was performed with 10%−10% A from 0 to 3 min, 10%−90% A from 3 to 10 min, and 90%−90% A from 10 to 13 min. The column was maintained at room temperature. The flow rate was set at 1.0 mL/min. The detection wavelength was 254 nm, and the injection volume was 10 μL.

2.8. Renal clearance efficiencies and in vivo stability studies

Female BALB/c mice were intravenously injected with the HD3-CD (0.5 mmol/L, 100 μL) or orally gavaged with HD6 (0.3 mmol/L, 200 μL, dissolved in 1% DMSO) and placed in metabolic cages for collecting urine and faecal samples. Urine and faeces were collected within 12 h of post-injection. Urine was freeze-dried and dissolved with 100 μL H_2O, and faeces were extracted in MeOH. After that, the mixture was quantified and analyzed by HPLC (Thermo) and ESI (Waters).

2.9. Real-time in vivo NIR-II imaging of kidney and liver dysfunction

After mice were treated with cisplatin (20 mg/kg body weight) or PBS at t = 72 h, real-time NIR imaging from dorsal and ventral views was conducted at t = 0.3, 1, 3, 5, 7, or 9 h after intravenous injection of HD3-CD (0.5 mmol/L, 60 μL, dissolved in PBS). Fluorescence images were conducted using the MARS spectrum imaging system (Artemis Intelligent) with an acquisition time of 100 ms at a power density of 0.8 W/cm^2 (880 nm laser, 1000 nm long-pass filter). Finally, the fluorescence normalized intensity of the kidney and liver was calculated according to the imaging datasets.

2.10. Real-time in vivo NIR-II imaging of gastric emptying disorder

After mice were treated with cisplatin (20 mg/kg body weight) or PBS at t = 72 h, real-time NIR imaging was conducted at t = 0.1, 0.5, 1,3, 5 or 7 h after orally administering HD6 (0.3 mmol/L, 200 μL, dissolved in 1% DMSO). Fluorescence images were conducted using the MARS spectrum imaging system (Artemis Intelligent) with an acquisition time of 50 ms at a power density of 0.2 W/cm^2 (660 nm laser, 1000 nm long-pass filter). Finally, the fluorescence area (t = 0.1 h) or fluorescence intensity of the stomach was calculated according to the imaging datasets.

2.11. Real-time in vivo NIR-II imaging of intestinal injury

After mice were treated with cisplatin (20 mg/kg body weight) at $t = 24$, 48, 72, or 84 h, real-time NIR imaging was conducted after intraperitoneal injection of HD14 (0.2 mmol/L, 100 μL, dissolved in 1% DMSO). Fluorescence images were performed using the MARS spectrum imaging system (Artemis Intelligent) with an acquisition time of 100 ms at a power density of 1 W/cm^2 (915 nm laser, 1050 nm long-pass filter). Finally, the fluorescence area of the ileocecal valve was calculated according to the imaging datasets.

2.12. In vivo dual-color imaging of liver and stomach or kidney and stomach

Female BALB/c mice were treated with cisplatin (20 mg/kg body weight) and PBS at $t = 72$ h. Following an intravenous injection of HD3-CD (0.5 mmol/L, 60 μL, dissolved in PBS), the mice were permitted to move freely for 0.3 h. Subsequently, the mice were orally administered with HD6 (0.3 mmol/L, 200 μL, dissolved in 1% DMSO). Fluorescence images were conducted using the MARS spectrum imaging system (Artemis Intelligent) with the excitation of 808 nm (1000 nm long-pass filter, 0.8 W/cm^2) and 660 nm (1000 nm long-pass filter, 0.2 W/cm^2) laser successively at different time points (0.3, 1, 3, 5, 7, or 9 h).

2.13. In vivo three-color imaging of liver, stomach, and intestine

Female BALB/c mice were treated with cisplatin (20 mg/kg body weight) or PBS at $t = 72$ h. Following an intravenous injection of HD3-CD (0.5 mmol/L, 60 μL, dissolved in PBS), the mice were permitted to move freely for 0.3 h. Subsequently, the mice were orally administered with HD6 (0.3 mmol/L, 200 μL, dissolved in 1% DMSO) and intraperitoneal injected with HD14 (0.2 mmol/L, 100 μL, dissolved in 1% DMSO). Fluorescence images were conducted using the MARS spectrum imaging system (Artemis Intelligent) with the excitation of 808 nm (1000 nm long-pass filter, 0.8 W/cm^2), 660 nm (1000 nm long-pass filter, 0.2 W/cm^2) and 915 nm (1050 nm long-pass filter, 1.0 W/cm^2) laser line.

2.14. Western blot analysis

The tissues were lysed using RIPA buffer (Beyotime Biotechnology, Shanghai, China) containing 1 mmol/L PMSF (Solarbio, Beijing, China) for 20 min on ice. The protein content was determined by a BCA protein assay kit (Yuanye Biotechnology, No. R21250). Briefly, proteins (25−50 μg) were subjected to SDS-PAGE (10%−15%), followed by being transferred to PVDF membrane (Millipore, Massachusetts, USA). After blocking with 5% non-fat milk for 2 h at room temperature, the membranes were incubated with antibodies including β-actin (1:2000), NLRP3 (1:1000), TGF-β1 (1:2000), NF-κB (1:1000), SMAD3 (1:5000) and BAX (1:2000) at 4 °C overnight. Thereafter, the membranes were rinsed with TBST 5 times (5 min/time) and incubated with HRP-conjugated secondary antibodies (1:2000) at room temperature for 2 h. Finally, the bands were observed using BeyoECL Plus solution (No. P0018S, Beyotime, China) by gel imaging analysis system (Tanon 4600SF, Shanghai, China). The protein expression was quantified by ImageJ software (National Institutes of Health, Maryland, USA). β-Actin was used as the internal reference.

2.15. Statistical analysis

The *in vitro*, *in vivo*, and *ex vivo* fluorescence signals were quantified with region of interest analysis using Living Image software (National Institutes of Health, Maryland, USA). Statistical analyses were performed using GraphPad Prism 9.0 (GraphPad Software). Data were expressed as the mean ± standard deviation (SD) unless stated otherwise. Statistical differences between the two groups were tested with a two-tailed Student's *t*-test. For all tests, P values less than 0.05 were considered statistically significant ($^*P < 0.05$, $^{**}P < 0.01$ and $^{***}P < 0.001$).

3. Results and discussion

3.1. Design, synthesis, and photophysical characterization

Enhancing conjugation is an effective way to redshift the emission wavelength. We designed three transformation strategies based on the classical D−π−A structure of HDs. First, extending the conjugate system of the terminal moiety introduced the furan-benzo[cd]indol, which drives the emission to the NIR-II window. Second, substituting the heteroatom (X) from oxygen (O) to sulfur (S), selenium (Se), and silicon (Si) is anticipated to achieve a greater redshift. Finally, varying the substitution patterns (such as hydroxyl and ethylenediamine) in the terminal heterocycles allows for fine-tuning, enabling the customization of appropriate fluorophores for NIR-II multiplexed imaging. This strategy resulted in the development of 14 spectrally distinct and compatible fluorophores (Fig. 2A). All HDs can be synthesized through two robust routes: (i) derivatives of the xanthene skeleton were combined with various indole compounds to produce HD1−10 and HD13−14. (ii) Cyanine ET-1080 condensates with 3-hydroxythiophenol or species 3 to form HD11−12. Detailed synthesis and characterization of HDs are presented in the Supporting Information. The purity of all dyes is >95%.

The photophysical properties of HDs were examined in methanol, summarized in Fig. 2A and Supporting Information Fig. S1. The spectrum of HDs covered the region between the NIR-I and NIR-II windows, with the values ranging from 659 to 988 nm (maximum absorption, λ^{max}_{abs}) and 674 nm−1145 nm (maximum emission, λ^{max}_{em}), showing promising imaging prospects (Fig. 2B−G). Compared with HD1 (676 nm), the λ^{max}_{em} of HD2 (780 nm), HD3 (850 nm), HD4 (840 nm), and HD5 (830 nm) are redshifted 104, 174, 164, and 154 nm, respectively. Suggesting that extending conjugation is an effective method to enhance imaging performance. The replacement of heteroatoms (O, S, Se, Si) leads to a redshift in λ^{max}_{em} from HD3 (850 nm) to HD11 (855 nm), HD12 (880 nm), and HD13 (944 nm) by 5, 30, and 94 nm, respectively. Indicating that silicon substitution (HD13) improves spectroscopic redshift efficiency more than selenium, sulfur, and oxygen. However, the presence of inter- and para-substituted hydroxyl groups on the phenyl rings has minimal impact on λ^{max}_{em}. Additionally, based on previous experience[44,45], the integration of both furan-benzo[cd]indole and ethylenediamine portions in the HD14 domain resulted in a redshift of its λ^{max}_{em} to 1145 nm, which is an unusually long wavelength for the HD family. It is also important to note that the silicon atom substitutions in HD13 (235 nm) and HD14 (157 nm) produce significant Stokes shifts, which can effectively minimize the interference from excitation light.

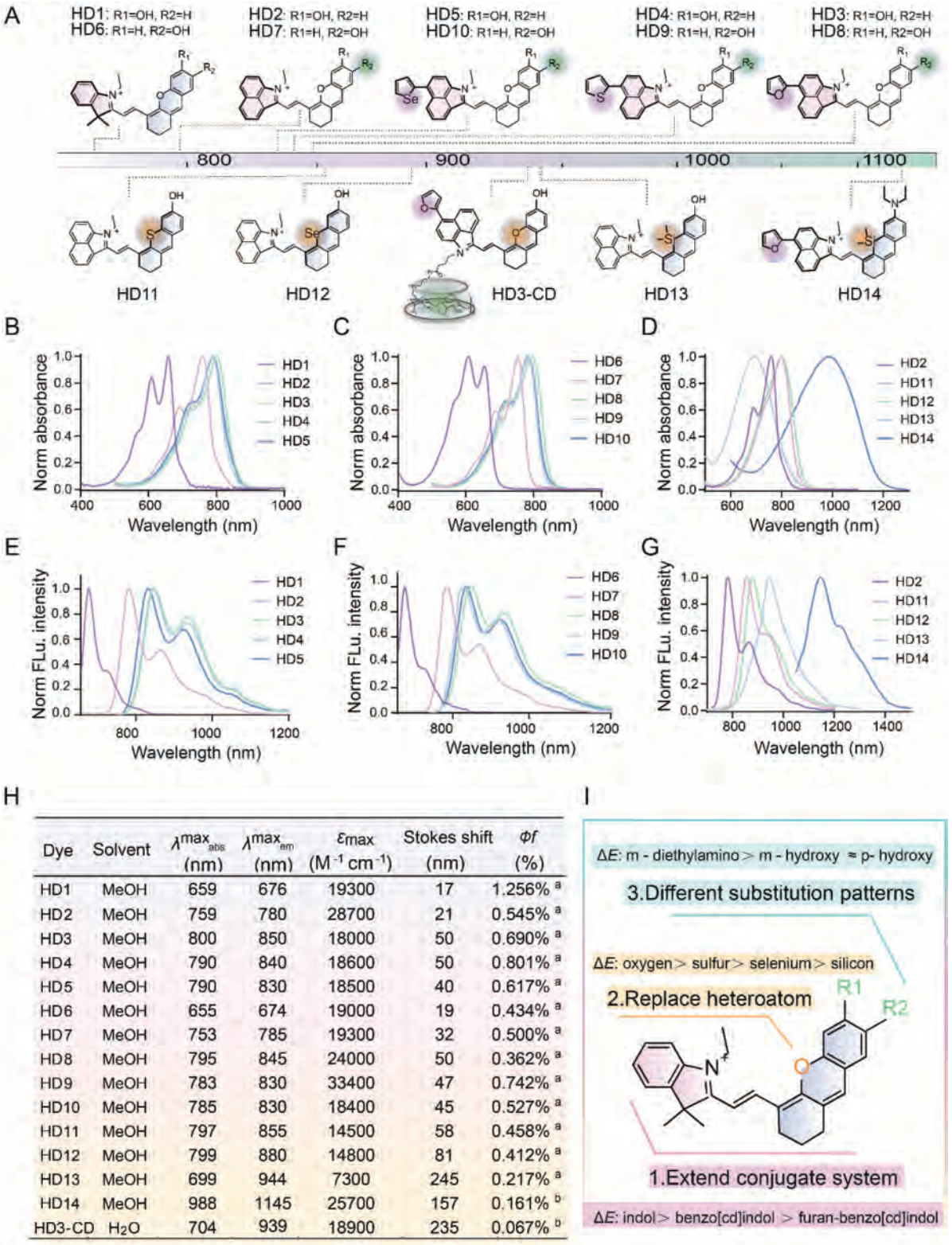

Dye	Solvent	λ^{max}_{abs} (nm)	λ^{max}_{em} (nm)	ε_{max} ($M^{-1}\,cm^{-1}$)	Stokes shift (nm)	Φf (%)
HD1	MeOH	659	676	19300	17	1.256% [a]
HD2	MeOH	759	780	28700	21	0.545% [a]
HD3	MeOH	800	850	18000	50	0.690% [a]
HD4	MeOH	790	840	18600	50	0.801% [a]
HD5	MeOH	790	830	18500	40	0.617% [a]
HD6	MeOH	655	674	19000	19	0.434% [a]
HD7	MeOH	753	785	19300	32	0.500% [a]
HD8	MeOH	795	845	24000	50	0.362% [a]
HD9	MeOH	783	830	33400	47	0.742% [a]
HD10	MeOH	785	830	18400	45	0.527% [a]
HD11	MeOH	797	855	14500	58	0.458% [a]
HD12	MeOH	799	880	14800	81	0.412% [a]
HD13	MeOH	699	944	7300	245	0.217% [a]
HD14	MeOH	988	1145	25700	157	0.161% [b]
HD3-CD	H_2O	704	939	18900	235	0.067% [b]

Figure 2 Physical and chemical properties of HDs. (A) HDs' chemical structures and fluorescence peak distribution. (B−D) The absorption spectrum of HDs in methanol solution. (E−G) The emission spectrum of HDs in methanol solution. (H) The photophysical data for HDs. [a]Fluorescence quantum yields were calculated relative to IR140 as the reference standard in ethanol ($\Phi f = 0.167$); [b]Fluorescence quantum yields were calculated relative to IR26 as the reference standard in DCE ($\Phi f = 0.5\%$). (I) Structure−optical property relationship.

To understand the effect of the modification strategy on the spectral shifts, density-functional theory (DFT) calculations were performed (Supporting Information Fig. S2). The highest occupied molecular orbital (HOMO)/lowest unoccupied molecular orbital (LUMO) energy gaps for HD1 to HD5 are 2.47, 2.09, 1.93, 1.99, and 1.99, respectively, indicating a trend that aligns with the observed wavelength shifts. The reduction in HOMO/LUMO energy gaps from HD2 (2.09) to HD11 (2.02), HD12 (1.99) and HD13 (1.89) supports the design approach of achieving redshifts through heteroatom substitution, while HD14, with the lowest energy gap of 1.71, highlights the significant role of the furyl-benzo[cd]indole and ethylenediamine components in the spectral redshift. Given these structure−property relationships, the HDs demonstrate strong potential for imaging applications, and we anticipate that they could aid in drug toxicity monitoring. Based on the above data, we proposed the structure-optical property relationship of the HDs (Fig. 2H and I). Generally, adjusting the HOMO−LUMO gap (ΔE) is the most straightforward method to modify the emission wavelength of the fluorophore. Expanding the conjugated π structure can significantly reduce the HOMO−LUMO gap and redshift the emission spectrum[34]. For instance, when the donor changes from indole to benzo[cd]indole and then to furan-benzo[cd]indole, the emission wavelength shifts from 676 nm (HD1) to 850 nm (HD3). Additionally, heteroatom exchange is also a practical molecular engineering strategy to shift the emission wavelength bathochromically. In general, replacing the bridging oxygen with less electron-donating atoms, such as elements of (S, Se, Si), can redshift the emission of dyes to deep red, or even near-infrared regions, due to the stabilization of LUMO energy levels through a $\sigma^*-\pi^*$ conjugation between heteroatoms σ^* orbitals and a π^* orbital of fluorophore[29]. Furthermore, for D−π−A fluorophores, increasing the electron density of the electron-donating group usually enhances the intramolecular charge transfer (ICT) effect, resulting in a smaller HOMO−LUMO gap[46]. The diethylamino substituent has a stronger electron-donating ability than the meta- or *para*-hydroxyl groups. Integrating the above methods provides a feasible path for developing fluorophores with longer wavelengths. Combining the effects of enlarging the conjugate π structure and heteroatoms or the electron-donating capability of the terminal moiety can further promote the $\lambda^{max}{}_{em}$ of HDs from 676 nm (HD1) to 1145 nm (HD14) NIR-II region.

3.2. Real-time in vivo NIR-II imaging of kidney and liver dysfunction

Hepatic and kidney dysfunctions are frequent side effects of medications. Monitoring these dysfunctions is crucial to prevent nephrotoxic or hepatotoxic drugs from being released into the market. One of the main challenges in real-time optical imaging of kidney and liver function is creating optical agents that have both high renal clearance and water solubility. Inspired by a previous study[47,48], we attempted to combine a fluorophore moiety with a renal-clearance-enabling moiety. After considering the imaging capabilities and the adaptable structure, we chose HD3 as the base for modification to create HD3-CAR, which includes a carboxy group. Ultimately, HD3-CAR was combined with a renal-clearance-enhancing component (mono-(6-(1,6-hexamethylenediamine)-6-deoxy)-β-cyclodextrin, HeβCD) to produce HD3-CD. This compound was characterized using HPLC, HRMS, and MALDI-TOF; the synthesis process is detailed in the Supporting Information

The $\lambda^{max}{}_{abs}$ of HD3-CD in water is 704 nm, and the $\lambda^{max}{}_{em}$ is 939 nm; in methanol, the $\lambda^{max}{}_{abs}$ 803 nm, the $\lambda^{max}{}_{em}$ is 940 nm (Supporting Information Fig. S3A and S3B). The $\lambda^{max}{}_{abs}$ in water exhibit a 99 nm blue shift compared to that in methanol, which we speculate may be due to the formation of H-aggregates through intermolecular $\pi-\pi$ stacking (Fig. S3C). To investigate this, we studied the absorption and fluorescence spectra of HD3-CD in methanol−water mixed solutions with varying water volume fractions. The results show that as the water content increases from 10% to 100%, the absorption peak at 803 nm significantly decreases (Fig. S3D). Simultaneously, the NIR-II fluorescence intensity gradually weakens with increasing water content, confirming that HD3-CD forms H-aggregates in water due to π-π interactions (Fig. S3E). To assess its potential for time-lapse bioimaging, the photostability of HD3-CD was examined. Compared to the commercial dye ICG, HD3-CD demonstrated better photostability, showing negligible absorption intensity decay when exposed to a continuous 808 nm laser for 30 min (Fig. S3F−S3H). Additionally, HD3-CD displayed excellent imaging capabilities; a dye-filled capillary submerged in 1% intralipid was successfully imaged under 808 nm excitation, revealing clear features even at a depth of 4 mm (Supporting Information Fig. S4A−S4F). Further whole-body fluorescence imaging with HD3-CD showed intense fluorescence signals in the mice liver (ventral view) and kidneys (dorsal view). HPLC analysis of recovered urine revealed that the metabolic ratio in the kidney after 12 h was 3.64 ± 0.3% (Supporting Information Fig. S5A and S5B). Furthermore, hematoxylin and eosin (H&E) staining of the tissues indicated that HD3-CD did not result in any tissue damage after 24 h of injection, suggesting it has good biocompatibility (Supporting Information Fig. S6).

Based on our findings, we assessed the effectiveness of HD3-CD in monitoring liver and kidney dysfunctions. Cisplatin, a prominent chemotherapy agent, is known for its strong therapeutic benefits but also for significant side effects. We conducted real-time monitoring of liver and kidney dysfunctions during cisplatin chemotherapy using *in vivo* imaging techniques. After administering cisplatin (20 mg/kg, 72 h), HD3-CD was injected intravenously into mice, and imaging was performed in the NIR-II window at various intervals. As shown in Fig. 3A, the signal profiles in both the kidneys and liver at 72 h post-cisplatin treatment were markedly different from those in the saline-treated control group. The rate of signal decline in the kidneys of the cisplatin-treated mice (0.07 ± 0.06 and 0.47 ± 0.04 at 1 and 9 h post-injection of HD3-CD, respectively) was slower compared to the saline-treated mice (0.31 ± 0.09 and 0.63 ± 0.05 at 3 and 9 h post-injection of HD3-CD, respectively), indicating retention of HD3-CD in the kidneys (Fig. 3B). Similarly, the signal reduction rate in the liver of the cisplatin group was 0.11 ± 0.2 at 5 h and 0.24 ± 0.05 at 9 h, which was lower than the control group's rates of 0.24 ± 0.04 at 5 h and 0.39 ± 0.04 at 9 h (Fig. 3C). This slower clearance in the liver was attributed to damage caused by cisplatin treatment after 72 h. These findings were further validated through pathological (Supporting Information Fig. S7A and S7B) and blood biochemical analyses (Fig. 3D and E), indicating that HD3-CD can noninvasively monitor kidney and liver dysfunctions using NIR-II imaging.

3.3. Real-time in vivo NIR-II imaging of gastric emptying disorder

Cisplatin is also associated with frequent gastrointestinal side effects. The strong gastrointestinal toxicity weakens the

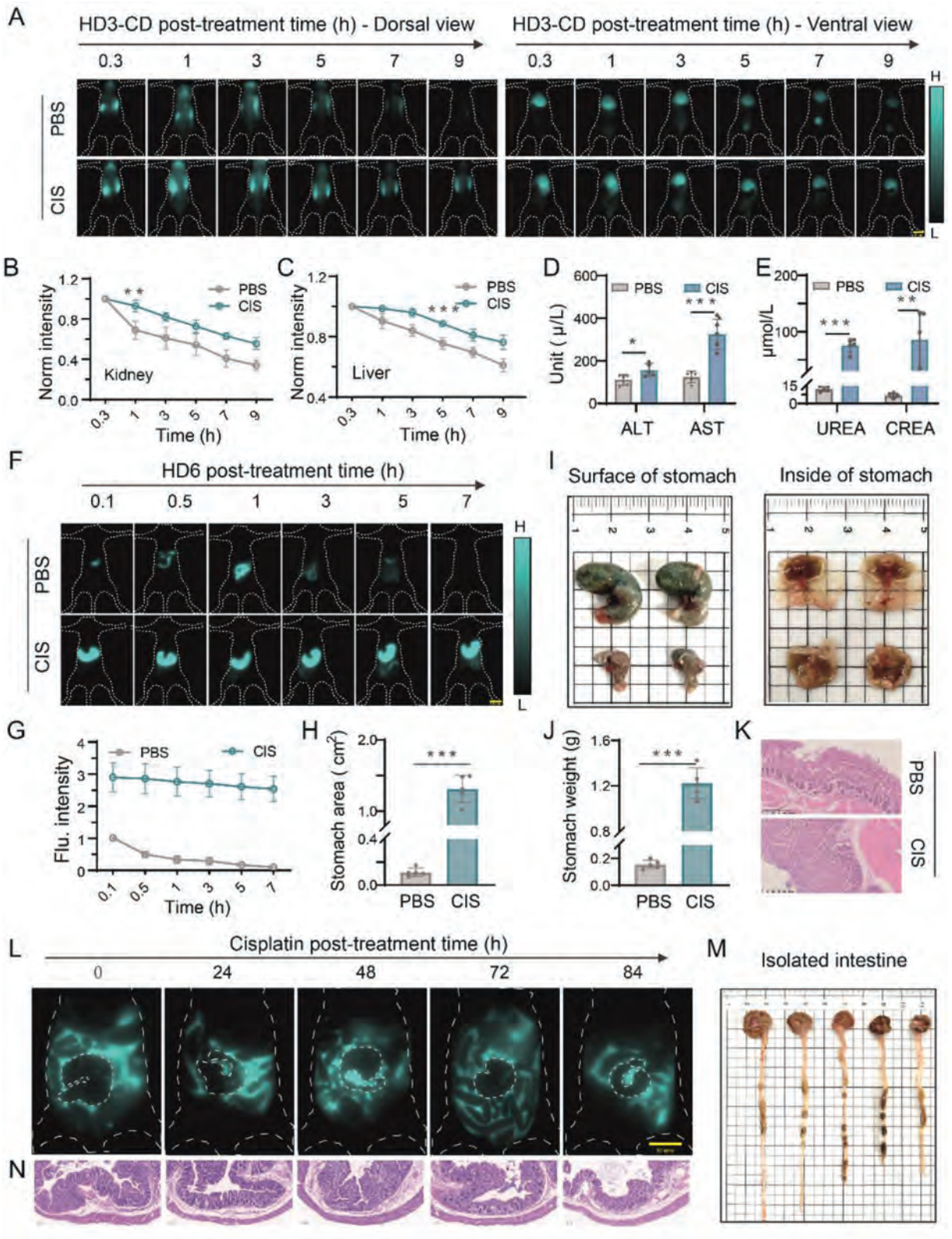

Figure 3 Real-time *in vivo* NIR-II imaging. (A) Representative NIR-II images from dorsal and ventral views of living mice after intravenous injection of HD3-CD under 808 nm excitation, scale bar = 10 mm. (B, C) Analysis of kidney and liver fluorescence normalized intensity during the monitoring time. (D, E) Analysis of blood biochemical index. (F) Representative NIR-II images of living mice after orally HD6 under 660 nm excitation, scale bar = 10 mm. (G) Analysis of gastric fluorescence intensity during the monitoring time. (H) Analysis of gastric fluorescence area at $t = 0.1$ h. (I, J) Isolated stomach and weights. (K) H&E staining images of stomach, scale bar = 250 μm. (L) Representative NIR-II images of living mice after intraperitoneal injection of HD14 under 915 nm excitation, scale bar = 10 mm. (M) Isolated intestine. (N) H&E staining images of intestine, scale bar = 100 μm. Data are presented as mean ± SD ($n = 5$). *$P < 0.05$, **$P < 0.01$, ***$P < 0.001$. ns, not significant.

enthusiasm of patients to treat their diseases. We tried to establish a more secure and convenient NIR-II gastrointestinal imaging monitoring mode than mainstream techniques like barium swallow and endoscopy. It is challenging to maintain probe integrity and imaging quality in a complicated digestive microenvironment containing digestive juices and gastric acid. We tested the HDs series probes in pH 2−7 phosphate-buffered saline (PBS, simulated gastric juice) to observe changes in their absorption (Supporting Information Fig. S8). The results showed that HD6, HD7, and HD8 maintained a stable absorption intensity in acidic conditions. Surprisingly, HD6 exhibited a well-spaced spectrum with HD3-CD, which provided a solid basis for multiplexed imaging.

The $\lambda^{max}{}_{abs}$ of HD6 in 1% DMSO is 645 nm, the $\lambda^{max}{}_{em}$ is 671 nm, and the tail of the HD6 fluorescent spectrum extends to the NIR-II region (Supporting Information Fig. S9A). When exposed to a 660 nm laser, HD6 demonstrated reliable light stability (Fig. S9B−S9D) and a penetration depth exceeding 3 mm, indicating promising imaging potential (Supporting Information Fig. S10A−S10F). After oral administration of HD6 into mice, the stomach, ileum, cecum, and rectum appeared successively over time and were wholly excreted with faeces (Supporting Information Fig. S11). To assess the *in vivo* stability of HD6, we analyzed the optical and chemical properties of HD6 recovered from faeces and compared them to the pure form. The absorption, HPLC, and mass spectra of excreted HD6 in the faeces were nearly identical to those of pure HD6 (Supporting Information Fig. S12A−S12D). The H&E staining images demonstrated that HD6 exhibited minimal toxicity to the heart, liver, spleen, lung, kidneys, stomach, and intestine while effectively maintaining NIR-II signaling in the gastrointestinal microenvironment (Fig. S6).

Motivated by these studies, we tried to monitor gastric emptying disorders during cisplatin chemotherapy using HD6. The HD6 was administered orally to mice (which had been fasted for 8 h prior), followed by treatment with cisplatin (20 mg/kg, 72 h), and was then imaged *in vivo* using NIR-II imaging at a 660 nm laser. As shown in Fig. 3F, the gastric signal in the saline control group gradually diminished during the monitoring period, while the intestinal fluorescence signal began to emerge. In contrast, the cisplatin treatment group maintained a relatively strong gastric fluorescence signal with a weak intestinal signal. Calculations indicated that at 3 and 9 h post-administration of HD6, the gastric fluorescence intensity in the cisplatin-treated group was 9.2 and 25.2 times greater than that of the control mice, respectively (Fig. 3G). Furthermore, cisplatin treatment resulted in a notable accumulation of food in the stomach, with the stomach fluorescence area of cisplatin-treated mice being 11.8 times larger than that of the saline control group at 0.1 h (Fig. 3H). These findings were corroborated by *ex vivo* gastric tissue and pathological sections (Fig. 3I−K). Overall, these results suggest that HD6 can effectively and noninvasively monitor gastric emptying dysfunction using NIR-II imaging.

3.4. Real-time in vivo NIR-II imaging of intestinal injury

The previously mentioned method successfully visualizes the gastrointestinal tract in healthy mice. However, a significant gastric emptying issue hinders most HD6 from effectively entering the intestine, resulting in a considerable loss of intestinal data in the cisplatin group. We hope to introduce new monitoring techniques to observe the intricate structure of the gut. Notably, HD14 showed the highest redshift among the HD family, with a $\lambda^{max}{}_{abs}$ of 954 nm and a $\lambda^{max}{}_{em}$ of 1105 nm in 1% DMSO (Supporting Information Fig. S13A). When exposed to a 915 nm laser, HD14 exhibited consistent light stability (Fig. S13B) and could penetrate more than 5 mm (Supporting Information Fig. S14A−S14G). Additionally, it demonstrated effective spectral separation from HD6 and HD3-CD, enabling the possibility of multiplexed imaging. After intraperitoneal injection of HD14 in mice, no significant abnormalities or injuries were observed in the major organs, suggesting that HD14 is safe for use and suitable for *in vivo* imaging (Fig. S6). Crucially, the *in vivo* imaging results showed excellent correlation with *ex vivo* intestinal anatomy (Supporting Information Fig. S15), with negligible interference from intestinal peristalsis throughout the imaging window (Supporting Information Video S1). To assess the intestinal damage caused by cisplatin, HD14 was injected intraperitoneally at various time intervals after cisplatin treatment (24, 48, 72, and 84 h), and *in vivo* imaging was conducted using 915 nm excitation (Fig. 3L). The results indicated a gradual reduction in the ileocecal valve as the duration of cisplatin treatment increased. The area of the ileocecal valve in the cisplatin group after 84 h was only 0.46 times that of the control group. This finding was supported by *ex vivo* intestinal tissue analysis (Fig. 3M). Furthermore, H&E staining demonstrated significant mucosal damage and crypt loss in the colon tissue of the cisplatin treatment group (Fig. 3N). These findings suggest that HD14 can effectively monitor intestinal damage induced by cisplatin through NIR-II imaging.

3.5. NIR-II multiplexed imaging

Benefiting from the well-spaced spectra of HD6, HD3-CD, and HD14, NIR-II-based multiplexed imaging for monitoring multi-organ damage becomes possible. The absorption bands of HD6, HD3-CD, and HD14 are spectrally separated by nearly 200 nm (Fig. 4A). Therefore, they could be orthogonally excited by 660, 808, and 915 nm with minimal crosstalk, as demonstrated by imaging their organic and aqueous solutions in Eppendorf tubes. Excitation at 660 nm yielded the fluorescence intensity ratios of 82.0/9.8/8.2 in the organic solvent and 76.4/9.4/14.2 in the aqueous solution, favoring HD6. Excitation at 808 nm, the fluorescence intensity ratios were 1.5/80.5/18 in organic solvent and 2.2/66.8/31.0 in aqueous solution, favoring HD3-CD. Excitation at 915 nm resulted in fluorescence intensity ratios of 9.2/11.9/78.9 in organic solvent and 1.7/23.6/74.7 in aqueous solution, favoring HD14 (Fig. 4B). Following this, we performed dual-color imaging on mice treated with PBS or cisplatin. This imaging method combined HD6 (channel 1) and HD3-CD (channel 2) with individual excitations at 660 and 808 nm, respectively. The technique enabled long-term, high-contrast visual monitoring of the gastrointestinal tract, liver, and kidneys, starting with intravenous injection of HD3-CD followed by oral administration of HD6 (Fig. 4C). At 0.3 h, the PBS and cisplatin treatment groups showed clear separation of the stomach and liver with high signal-to-noise ratio (SNR) resolutions of 2.7 and 10.7 (abdominal view), and the stomach and kidney with resolutions of 3.0 and 21.8 (dorsal view) (Supporting Information Fig. S16A). Furthermore, the metabolic characteristics of the liver, kidney, and gastrointestinal tract observed through this technology in PBS and cisplatin-treated mice were highly consistent with previous research. Therefore, we believe this dual-color imaging technique offers a novel approach for monitoring multi-organ damage.

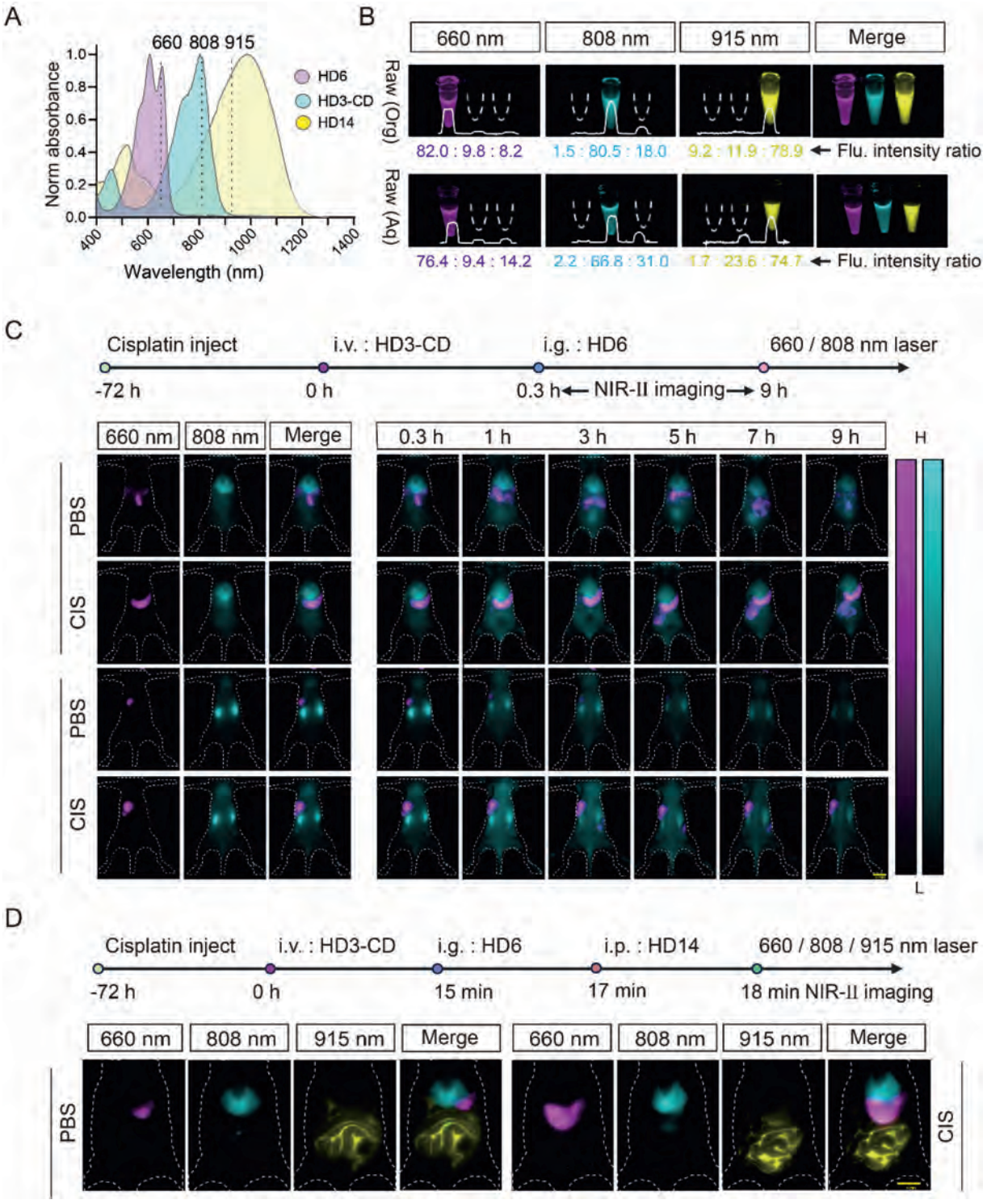

Figure 4 NIR-II multiplexed imaging. (A) Normalized absorption spectra of HD6, HD-CD, and HD14 in MeOH solution. (B) Fluorescence images of the PBS and MeOH solutions of HD6, HD-CD, and HD14 in EP tubes with 660, 808, and 915 nm excitation, respectively. (C) Schematic illustration showing the dual-color imaging protocol for stomach and liver (ventral view) or stomach and kidney (dorsal view). (D) Schematic illustration showing the three-color imaging protocol for the stomach, intestine, and liver. i.v.: intravenous injection, i.p.: intraperitoneal injection, i.g.: intragastric gavage, HD6: magenta pseudo-color, HD3-CD: cyan pseudo-color, HD14: yellow pseudo-color. Scale bar = 10 mm.

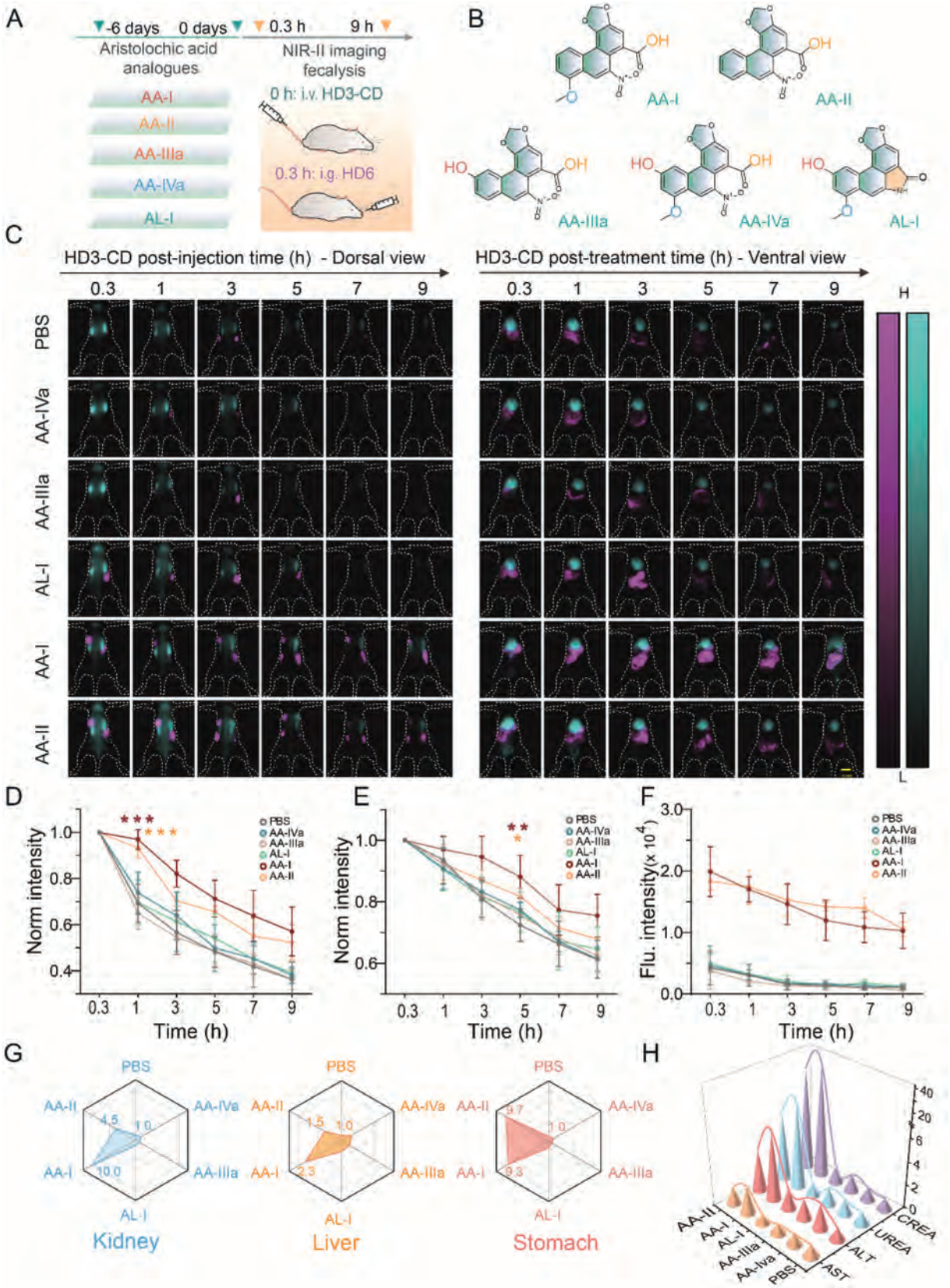

Figure 5 Real-time NIR-II imaging and analysis of AAs-induced multi-organ damage. (A) Schematic illustration of the timeline of AAs therapy. (B) The chemical structures of AAs. (C) Representative NIR-II images from dorsal and ventral views of living mice after oral gavage of AAs. HD6: magenta pseudo-color, HD3-CD: cyan pseudo-color. (D−F) Analysis of kidney, liver, and stomach fluorescence intensity during the monitoring time. (G) Analysis of NIR-II signal changes in the liver (t = 5 h), kidney (t = 1 h), and stomach (t = 3 h). (H) Analysis of blood biochemical changes. i.v.: intravenous injection, i.p.: intraperitoneal injection, i.g.: intragastric gavage. Data are presented as mean ± SD (n = 5). *P < 0.05, **P < 0.01, ***P < 0.001. ns, not significant. Scale bar = 10 mm.

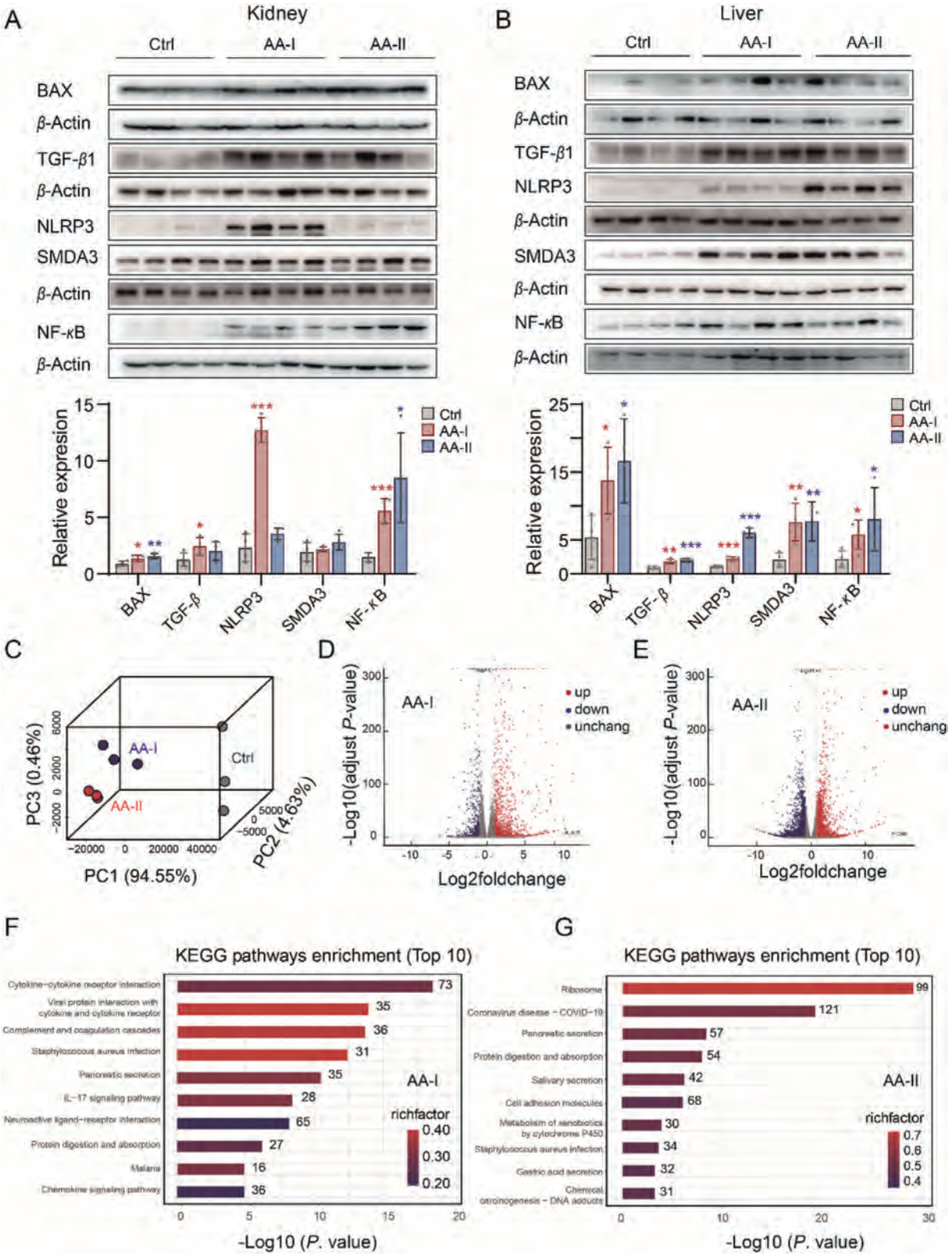

Figure 6 Western blot and transcriptome analysis of AA-I/II-induced liver, kidney, and stomach damage. (A, B) Expression of NF-κB, NLPR3, TGF-β, SMDA3, and BAX proteins in the kidney or liver of AA-I-, AA-II-treated mice. Data are presented as mean ± SD ($n = 4$). *$P < 0.05$, **$P < 0.01$, ***$P < 0.001$. ns, not significant. (C) Principal component analysis. (D, E) Analysis of differentially expressed genes. (F, G) KEGG enrichment analysis.

Moreover, we expanded this technique by using HD14 excited at 915 nm to enable three-color imaging. HD3-CD was administered via the tail vein, followed by an intragastric injection of HD6 and an intraperitoneal injection of HD14. As anticipated, the 915 nm (channel 3) was dedicated to HD14, clearly outlining the intestinal structure (Fig. 4D). In the control and cisplatin treatment groups, the liver and intestine were separated by SNR of 11.1 and 14.0, respectively, and the stomach and intestine were separated by SNR of 4.6 and 4.2, respectively (Fig. S16B).

Compared with dual-color imaging, three-color imaging provides more comprehensive organ information and solves the issue of missing imaging data due to disease. Nonetheless, the long-term monitoring capability of the three-channel imaging technology is inferior to that of the two-channel imaging due to intestinal movement and the gradual absorption of HD14. In summary, we have established an optional multi-channel multiplexing imaging technology conducive to exploring the potential multi-organ toxicity of drugs and accelerating drug development.

3.6. In vivo multiplexed NIR-II imaging of AAs-induced multiple organ dysfunction

Aristolochic acids (AAs) are toxic compounds found in Aristolochiaceae plants and have been found to induce aristolochic acid nephropathy. These plants were initially used as herbal remedies for weight loss and have not been extensively studied for their gastrointestinal toxicity, which has piqued our interest in AAs. We expect to provide effective evidence for the discovery of more potential toxicity of AAs through the use of two-color imaging technology. Mice were orally administered with representative AAs (20 mg/kg), including AA-I, AA-II, aristolochic acid IIIa (AA-IIIa), aristolochic acid IVa (AA-IVa), and aristolactam I (AL-I), and PBS as the control group. After 6 days of treatment, HD3-CD was injected into the tail vein, and HD6 was intragastrically injected (Fig. 5A and B). NIR imaging was used to monitor signals from the kidneys, liver, and stomach (Fig. 5C). At 1 h post-injection of HD3-CD, NIR-II signals in decline in mice kidneys were 0.03 ± 0.04 (AA-I), 0.07 ± 0.04 (AA-II), 0.35 ± 0.07 (AA-IIIa), 0.26 ± 0.09 (AA-IVa), 0.30 ± 0.10 (AL-I), and 0.31 ± 0.08 (PBS), respectively. The renal clearance efficiency of AA-I and AA-II treatment groups was significantly lower than that of other treatment groups (Fig. 5D). At 5 h post-injection of HD3-CD, NIR-II signals the decline of liver in AA-I and AA-II treatment groups was 0.12 ± 0.07 and 0.18 ± 0.07, which was significantly lower than the control group (0.28 ± 0.05), AA-IIIa treatment group (0.24 ± 0.09), AA-IVa treatment group (0.23 ± 0.02), and AL-I treatment group (0.23 ± 0.06) (Fig. 5E). The gastric fluorescence signals in the AA-IIIa, AA-IVa, AL-I, or PBS treatment groups showed similar trends, while those in the AA-I and AA-II groups were consistently higher (Fig. 5F). For example, the fluorescence intensity at 3 h of AA-I and AA-II was 9.3 and 9.7 times greater than that of the control group, respectively. Fig. 5G summarizes the comparison of NIR-II signal changes in the liver ($t = 5$ h), kidney ($t = 1$ h), and stomach ($t = 3$ h) between the control group and the AAs treatment groups. The results showed that the probe clearance efficiency in the AA-I and AA-II groups was lower than in the AA-IIIa, AL-I, and PBS groups, indicating that AA-I and AA-II negatively impact the liver, kidneys, and stomach. Furthermore, we assessed the comparison of blood biochemical (Fig. 5H) and pathological (Supporting Information Fig. S17) between the control group and the AAs treatment groups. The results showed that the trend of liver, kidney, and stomach function injury was consistent with the clearance efficiency of the probe in different treatment groups. To our knowledge, this is the first instance of using dual-color imaging to identify potential gastric emptying disorders associated with AA-I and AA-II.

In addition, we analyzed the levels of proteins associated with inflammation (NF-κB, NLPR3), fibrosis (TGF-β, SMAD3), and apoptosis (BAX) in the livers and kidneys of mice treated with AA-I and AA-II using Western blot analysis. In the kidney, the expression of BAX, TGF-β, NLPR3, and NF-κB was elevated in the AA-I treated group, and that of BAX and NF-κB was elevated in the AA-II treated group, compared with the control group (Fig. 6A). In the liver, the expression of BAX, TGF-β, SMAD3, NLPR3, and NF-κB was elevated in both AA-I and AA-II treatment groups (Fig. 6B). In addition, we conducted a transcriptomic analysis of the stomachs from the AA-I and AA-II treated mice. Principal component analysis showed that samples were dispersed between groups and clustered within groups (Fig. 6C). The AA-I group had a total of 1936 differentially expressed genes compared to the control, with 1268 up-regulated and 668 down-regulated (Fig. 6D). The AA-II group had 5973 differentially expressed genes, with 2757 up-regulated and 3216 down-regulated (Fig. 6E). Kyoto Encyclopedia of Genes and Genomes (KEGG) enrichment analysis indicated that AA-I primarily affected signaling pathways related to cytokine−cytokine receptor interaction, viral protein interaction with cytokines and receptors, complement and coagulation cascades, IL-17 signaling pathway, protein digestion and absorption, and chemokine signaling pathway (Fig. 6F). In contrast, AA-II mainly influenced pathways such as ribosome, protein digestion and absorption, cell adhesion molecules, gastric acid secretion, and vascular smooth muscle contraction in gastric tissues (Fig. 6G). This suggests that exposure to AA-I and AA-II influenced the functional dynamics of the gastric.

4. Conclusions

In summary, we synthesized a series of HDs with harmonizable wavelengths according to the guidelines of physical organic chemistry. Among these, the representative dye HD14 stands out for its unusually long wavelength emission exceeding 1100 nm. From this library of HDs, we further created HD3-CD, characterized by its ability to clear from the liver and kidneys. It supported simultaneously evaluating cisplatin-induced organ damage, a topic that has not been previously explored. In addition, NIR-II imaging was evaluated for cisplatin-induced stomach and intestinal injury using HD6 (660 nm laser) and HD14 (808 nm laser), potentially broadening the monitoring of drug-induced side effects. The well-defined absorption spectra of HD3-CD, HD6, and HD14 enabled multicolor imaging with a high signal-to-noise ratio using NIR-II excitation in live mice. Notably, our multicolor imaging technique revealed potential gastric emptying issues related to AA-I and AA-II, which have not been documented before. We believe this study enhances optical multiplexing capabilities and opens new avenues for imaging multi-organ pathology in deep tissues while also providing an excellent multicolor imaging platform to investigate the potential toxicity of drugs.

Acknowledgments

This work was supported by the Science and Technology Commission of Shanghai Municipality (No. YDZX20233100004032001,

China), the Strategic Priority Research Program of the Chinese Academy of Sciences (No. XDB1040000, China), the National Natural Science Foundation of China (Nos. 32141005 and 82071976, China), the National Key Research and Development Program of China (No. 2023YFA1800804), Science and Technology Innovation Key R&D Program of Chongqing (No. CSTB2023TIAD-STX0006, China), the National Science and Technology Innovation 2030 Major Project of China (No. 2021ZD0203900).

Author contributions

Pu Jiang: Conceived the experiments and data curation and wrote the original draft. Ruihu Song: Data curation. Yue Hu: Data curation. Xin He: Project administration, supervision. Zhewei Zhang and Xuemei Wei: Supervision. Zhiming Wang: Probe synthesis. De-an Guo: Supervised the study and provided financial support via projects. Hao Chen: Supervised the study, conceived the experiments, and provided financial support via projects.

Conflicts of interest

The authors have no conflicts of interest to declare.

Appendix A. Supporting information

Supporting information to this article can be found online at https://doi.org/10.1016/j.apsb.2025.06.023.

References

1. Edwards IR, Aronson JK. Adverse drug reactions: definitions, diagnosis, and management. *Lancet* 2000;**356**:1255−9.
2. Andrade RJ, Chalasani N, Björnsson ES, Suzuki A, Kullak Ublick GA, Watkins PB, et al. Drug-induced liver injury. *Nat Rev Dis Primers* 2019;**5**:58.
3. Perazella MA, Rosner MH. Drug-induced acute kidney injury. *Clin J Am Soc Nephrol* 2022;**17**:1220−33.
4. Karamchandani DM, Westbrook L, Arnold CA. Drug-induced digestive tract injury: decoding some invisible offenders. *Hum Pathol* 2023; **132**:135−48.
5. Qi L, Luo Q, Zhang Y, Jia F, Zhao Y, Wang F. Advances in toxicological research of the anticancer drug cisplatin. *Chem Res Toxicol* 2019;**32**:1469−86.
6. McCrae JC, Morrison EE, MacIntyre IM, Dear JW, Webb DJ. Long-term adverse effects of paracetamol—a review. *Br J Clin Pharmacol* 2018;**84**:2218−30.
7. Zhao Y, Yin J, Zhang L, Zhang Y, Chen X. Drug−drug interaction prediction: databases, web servers and computational models. *Brief Bioinform* 2024;**25**:1−28.
8. Beierwaltes WH, Harrison-Bernard LM, Sullivan JC, Mattson DL. Assessment of renal function; clearance, the renal microcirculation, renal blood flow, and metabolic balance. *Compr Physiol* 2013;**3**: 165−200.
9. Cai Q, Zhu C, Yuan Y, Feng Q, Feng Y, Hao Y, et al. Development and validation of a prediction rule for estimating gastric cancer risk in the Chinese high-risk population: a nationwide multicentre study. *Gut* 2019;**68**:1576−87.
10. Senior JR. Alanine aminotransferase: a clinical and regulatory tool for detecting liver injury−past, present, and future. *Clin Pharmacol Ther* 2012;**92**:332−9.
11. Yang CT, Ghosh KK, Padmanabhan P, Langer O, Liu J, Eng DNC, et al. PET-MR and SPECT-MR multimodality probes: development and challenges. *Theranostics* 2018;**8**:6210−32.
12. Mezzanotte L, van 't Root M, Karatas H, Goun EA, Löwik CWGM. *In vivo* molecular bioluminescence imaging: new tools and applications. *Trends Biotechnol* 2017;**35**:640−52.
13. Jiang Y, Pu K. Molecular probes for autofluorescence-free optical imaging. *Chem Rev* 2021;**121**:13086−131.
14. Ntziachristos V, Ripoll J, Wang LV, Weissleder R. Looking and listening to light: the evolution of whole-body photonic imaging. *Nat Biotechnol* 2005;**23**:313−20.
15. Smith AM, Mancini MC, Nie S. Second window for *in vivo* imaging. *Nat Nanotechnol* 2009;**4**:710−1.
16. Antaris AL, Chen H, Diao S, Ma Z, Zhang Z, Zhu S, et al. A high quantum yield molecule-protein complex fluorophore for near-infrared II imaging. *Nat Commun* 2017;**8**:15269.
17. Hu Z, Fang C, Li B, Zhang Z, Cao C, Cai M, et al. First-in-human liver-tumour surgery guided by multispectral fluorescence imaging in the visible and near-infrared-I/II windows. *Nat Biomed Eng* 2019;**4**: 259−71.
18. Yu M, Zhou J, Du B, Ning X, Authement C, Gandee L, et al. Noninvasive staging of kidney dysfunction enabled by renal-clearable luminescent gold nanoparticles. *Angew Chem Int Ed Engl* 2016;**55**: 2787−91.
19. Dai S, Tao M, Zhong Y, Li Z, Liang J, Chen D, et al. In situ generation of red-to-NIR emissive radical cations in the stomach for gastrointestinal imaging. *Adv Mater* 2023;**35**:e2209940.
20. Cosco ED, Spearman AL, Ramakrishnan S, Lingg JGP, Saccomano M, Pengshung M, et al. Shortwave infrared polymethine fluorophores matched to excitation lasers enable non-invasive, multicolour *in vivo* imaging in real time. *Nat Chem* 2020;**12**:1123−30.
21. Ko J, Oh J, Ahmed MS, Carlson JCT, Weissleder R. Ultra-fast cycling for multiplexed cellular fluorescence imaging. *Angew Chem Int Ed Engl* 2020;**59**:6839−46.
22. Liu T-L, Upadhyayula S, Milkie DE, Singh V, Wang K, Swinburne IA, et al. Observing the cell in its native state: imaging subcellular dynamics in multicellular organisms. *Science* 2018;**360**:eaaq1392.
23. Hong G, Antaris AL, Dai H. Near-infrared fluorophores for biomedical imaging. *Nat Biomed Eng* 2017;**1**:10.
24. Wang S, Fan Y, Li D, Sun C, Lei Z, Lu L, et al. Anti-quenching NIR-II molecular fluorophores for *in vivo* high-contrast imaging and pH sensing. *Nat Commun* 2019;**10**:1058.
25. Bandi VG, Luciano MP, Saccomano M, Patel NL, Bischof TS, Lingg JGP, et al. Targeted multicolor *in vivo* imaging over 1,000 nm enabled by nonamethine cyanines. *Nat Methods* 2022;**19**:353−8.
26. Tian R, Ma H, Zhu S, Lau J, Ma R, Liu Y, et al. Multiplexed NIR-II probes for lymph node-invaded cancer detection and imaging-guided surgery. *Adv Mater* 2020;**32**:1907365.
27. Cheng HB, Cao X, Zhang S, Zhang K, Cheng Y, Wang J, et al. BODIPY as a multifunctional theranostic reagent in biomedicine: self-assembly, properties, and applications. *Adv Mater* 2023;**35**:2207546.
28. Samanta S, Lai K, Wu F, Liu Y, Cai S, Yang X, et al. Xanthene, cyanine, oxazine and BODIPY: the four pillars of the fluorophore empire for super-resolution bioimaging. *Chem Soc Rev* 2023;**52**: 7197−261.
29. Jiang G, Liu H, Liu H, Ke G, Ren TB, Xiong B, et al. Chemical approaches to optimize the properties of organic fluorophores for imaging and sensing. *Angew Chem Int Ed Engl* 2023;**63**:e202315217.
30. Ding F, Zhan Y, Lu X, Sun Y. Recent advances in near-infrared II fluorophores for multifunctional biomedical imaging. *Chem Sci* 2018; **9**:4370−80.
31. Ji A, Lou H, Qu C, Lu W, Hao Y, Li J, et al. Acceptor engineering for NIR-II dyes with high photochemical and biomedical performance. *Nat Commun* 2022;**13**:3815.
32. Wang S, Gai L, Chen Y, Ji X, Lu H, Guo Z. Mitochondria-targeted BODIPY dyes for small molecule recognition, bio-imaging and photodynamic therapy. *Chem Soc Rev* 2024;**53**:3976−4019.
33. Schneider L, Kalt M, Koch S, Sithamparanathan S, Villiger V, Mattiat J, et al. BODIPY-based photothermal agents with excellent phototoxic indices for cancer treatment. *J Am Chem Soc* 2023;**145**: 4534−44.

34. Ou YF, Ren TB, Yuan L, Zhang XB. Molecular design of NIR-II polymethine fluorophores for bioimaging and biosensing. *Chem Biomed Imaging* 2023;**1**:220−33.
35. Mishra ABR, Behera PK, Mishra BK, Behera GB. Cyanines during the 1990s: a review. *Chem Rev* 2020;**100**:1973−2012.
36. Zhu S, Hu Z, Tian R, Yung BC, Yang Q, Zhao S, et al. Repurposing cyanine NIR-I dyes accelerates clinical translation of near-infrared-II (NIR-II) bioimaging. *Adv Mater* 2018;**30**:1802546.
37. Nguyen A, Bhandari C, Keown M, Malkoochi A, Quaye M, Mahmoud D, et al. Increasing the dye payload of cetuximab-IRDye800CW enables photodynamic therapy. *Mol Pharm* 2024;**21**:3296−309.
38. Zeng Z, Liew SS, Wei X, Pu K. Hemicyanine-based near-infrared activatable probes for imaging and diagnosis of diseases. *Angew Chem Int Ed Engl* 2021;**60**:26454−75.
39. Liu Y, Diao S, Ruan B, Zhou Y, Yu M, Dong G, et al. Molecular engineering of activatable NIR-II hemicyanine reporters for early diagnosis and prognostic assessment of inflammatory bowel disease. *ACS Nano* 2024;**18**:8437−51.
40. Yuan L, Lin W, Zhao S, Gao W, Chen B, He L, et al. A unique approach to development of near-infrared fluorescent sensors for *in vivo* imaging. *J Am Chem Soc* 2012;**134**:13510−23.
41. Qin Z, Ren TB, Zhou H, Zhang X, He L, Li Z, et al. NIRII-HDs: a versatile platform for developing activatable NIR-II fluorogenic probes for reliable *in vivo* analyte sensing. *Angew Chem Int Ed Engl* 2022;**61**:e202201541.
42. Zhao L, Zhu H, Duo YY, Pang DW, Wang ZG, Liu SL. Near-Infrared II hemicyanine dye with large Stokes shift designed by TICT regulation for boosting imaging-guided photothermal therapy. *Adv Healthc Mater* 2023;**12**:e2301584.
43. Li H, Kim H, Xu F, Han J, Yao Q, Wang J, et al. Activity-based NIR fluorescent probes based on the versatile hemicyanine scaffold: design strategy, biomedical applications, and outlook. *Chem Soc Rev* 2022;**51**:1795−835.
44. East AK, Lee MC, Smaga LP, Jiang C, Mallojjala SC, Hirschi JS, et al. Synthesis of silicon-substituted hemicyanines for multimodal SWIR imaging. *Org Lett* 2022;**24**:8509−13.
45. Yao S, Chen Y, Ding W, Xu F, Liu Z, Li Y, et al. Single-atom engineering of hemicyanine and its amphiphilic derivative for optimized near infrared phototheranostics. *Chem Sci* 2023;**14**:1234−43.
46. Lei Z, Zhang F. Molecular engineering of NIR-II fluorophores for improved biomedical detection. *Angew Chem Int Ed Engl* 2021;**60**:16294−308.
47. Huang J, Xie C, Zhang X, Jiang Y, Li J, Fan Q, et al. Renal-clearable molecular semiconductor for second near-infrared fluorescence imaging of kidney dysfunction. *Angew Chem Int Ed Engl* 2019;**58**:15120−7.
48. Huang J, Li J, Lyu Y, Miao Q, Pu K. Molecular optical imaging probes for early diagnosis of drug-induced acute kidney injury. *Nat Mater* 2019;**18**:1133−43.